Available online at www.sciencedirect.com
ScienceDirect
Trans. Nonferrous Met. Soc. China 34(2024) 1759−1773
Transactions of Nonferrous Metals Society of China
www.tnmsc.cn

# Effect of Sc addition on downstream processing of twin-roll cast Al−Cu−Li−Mg−Zr-based alloys

Rostislav KRÁLÍK[1], Barbora KŘIVSKÁ[1], Lucia BAJTOŠOVÁ[1],
Mykhailo STOLBCHENKO[2], Mirko SCHAPER[2], Olexandr GRYDIN[2], Miroslav CIESLAR[1]

1. Department of Physics of Materials, Faculty of Mathematics and Physics, Charles University, Ke Karlovu 5, 12116, Prague, Czech Republic;
2. Department of Materials Science, Faculty of Mechanical Engineering, University of Paderborn, Warburger Straße 100, 33098, Paderborn, Germany

Received 31 January 2023; accepted 24 July 2023

**Abstract:** A processing scheme for preparing strips of Al−Cu−Li−Mg−Zr-based alloys microalloyed with Sc was proposed. This scheme includes a twin-roll casting of strips with a near-net-shaped 3 mm-thick gauge and a homogenization/solution treatment processing step. Two twin-roll cast Al−Cu−Li−Mg−Zr-based alloys were studied, one with an addition of 0.17 wt.% Sc, and the other without addition of Sc. Both alloys were annealed at 300 °C for 30 min, 450 °C for 30 min, and 530 °C for 30 min and quenched into room temperature water. The first two annealing steps provide a fine dispersion of $Al_3Zr$/$Al_3$(Sc,Zr) particles. The final annealing step serves as homogenization/solution treatment. A fine crystallization structure of the twin-roll cast materials enables the dissolution of primary particles containing the main alloying elements during a relatively short annealing time. Shorter soaking duration limits the depletion of surface layers from Li and significant coarsening of $Al_3Zr$/$Al_3$(Sc,Zr) dispersoids. The Sc-containing material has significantly finer grains already in the as-cast state. The $Al_3$(Sc,Zr) dispersoids formed during the homogenization/solution treatment step prevent grain coarsening at high temperatures. Strengthening $\theta'$($Al_2Cu$), $T_1$($Al_2CuLi$), and rare $S'$($Al_2CuMg$) phases are formed during subsequent artificial aging at 180 °C. The increase in yield strength was 200 MPa in the peak-aged conditions. This value is comparable to the ones reported in similar direct-chill cast materials, thus validating the proposed processing scheme.
**Key words:** microstructure; mechanical properties; Al−Cu−Li-based alloy; Sc alloying; twin-roll casting

## 1 Introduction

Al−Cu−Li−Mg-based alloys have been of high interest to the aerospace industry for their high specific mechanical properties. The current generation of Al−Cu−Li−Mg-based alloys contains a higher Cu/Li ratio, preventing the formation of metastable binary $Al_3Li$ precipitates [1]. They are strengthened mainly by plate-like phases of binary $\theta'$($Al_2Cu$) in $\{100\}_{Al}$ planes and ternary $T_1$($Al_2CuLi$) in $\{111\}_{Al}$ planes [2]. HAUSLER et al [3] showed that Al−Cu−Li−Mg alloys in the T6 temper (without pre-stretching prior to artificial aging) contain a much higher volume fraction of the $\theta'$ phase than the $T_1$ phase. Certain commonly added alloying elements like Ag or Mg could promote the precipitation of the $T_1$ phase. Additionally, Mg further decreases the total density of the alloy and can precipitate as a ternary $S'$ phase ($Al_2CuMg$) in the form of rods with a primary axis parallel to $[100]_{Al}$ directions [2].

**Corresponding author:** Rostislav KRÁLÍK, E-mail: rkralik96@gmail.com
DOI: 10.1016/S1003-6326(24)66505-2

Al−Cu−Li−Mg-based alloys are employed in the aerospace industry in the form of sheets as input material. They are generally rolled in multiple steps from direct-chill cast (DC-cast) ingots. DC-cast material processing requires a long holding time at high annealing temperatures during homogenization to properly dissolve coarse constituent particles formed during casting and homogenize solute distribution across the coarse structure [4]. Additionally, DC-cast material processing produces much waste due to the scalping of Li-depleted surface layers arising from Li evaporation at high homogenization temperatures [4,5]. Processed DC-cast AA2195 alloys generally reach micro-hardness values up to HV 200, yield strength around 560 MPa, and elongation to fracture at room temperature up to 12% [4,6,7]. DC-cast materials always contain Zr as a grain refining element. Zr has low diffusivity in Al and is resistant to coarsening during long standard annealing time. Temperatures above 400 °C usually facilitate the precipitation of the grain refining $Al_3Zr$ precipitate [8]. Another perspective grain refiner in Al alloys is Sc. It forms small $Al_3Sc$ coherent spherical particles in binary Al−Sc systems. Systems with Zr addition include a ternary $Al_3(Sc,Zr)$ phase [9]. The diffusivity of Sc in Al is higher than the diffusivity of Zr. Sc-containing phases form at lower annealing temperatures (typically 300 °C) and are more prone to coarsening [9,10]. This fact makes their addition to standard DC-cast Al−Cu−Li−Mg alloys questionable. The long, required annealing treatments can cause significant coarsening of the Sc-containing particles and degradation of their beneficial effects [11].

Several attempts to produce Al−Cu−Li−Mg strips show the possibility of preparing the material by an alternative twin-roll casting (TRC) method [12−14]. The higher solidification rate during TRC produces much finer grains, smaller constituent particles, and a more homogeneous macroscopic distribution of constituents [15]. Therefore, the necessary diffusion lengths for the solute redistribution and diffusion time for particle dissolution are lower in TRC materials. Thermal exposure of TRC alloys could be further reduced by combining homogenization and solution treatment into one step or a series of short steps. Additionally, shorter annealing treatments can reduce Li evaporation from the surface of the material. This effect might be particularly detrimental in sheet-shaped TRC materials [5]. A shorter annealing time allows $Al_3(Sc,Zr)$ particles to retain their beneficial effects. Multi-step heat treatment forming a finer $Al_3Sc$ core at lower temperatures and an $Al_3(Sc,Zr)$ shell at higher temperatures can also be beneficial to preventing $Al_3(Sc,Zr)$ coarsening [16]. The presented study describes the evolution of microstructure and mechanical properties of TRC strips processed by a novel route, maintaining the beneficial effect of Sc addition. Results are correlated with the same alloy without the Sc content. Materials investigated in the present study are two Al−Cu−Li−Mg−Zr alloys containing alloying elements in similar ratios as a standard AA2195 alloy but with a reduced concentration of main alloying elements. In contrast to previous attempts [12−14], the materials in this work contained Sc, and they were twin-roll cast with significantly lower final gauges, thus exploiting much shorter high-temperature treatments. Similar studies on TRC Sc-containing Al−Cu−Li−Mg−Zr alloys have never been done.

## 2 Experimental

TRC was performed using a laboratory twin-roll caster with rolls equipped with steel shells. The produced strips were approximately 3 mm in thickness and 20 cm in width. The casting process was described in more detail by GRYDIN et al [17]. The chemical composition of TRC materials (Table 1) was measured by the optical emission spectrometer (Q4 TASMAN). The materials are referred to as T and TSc for the Sc-free and Sc-containing materials, respectively.

Light optical microscopy (LOM) observations were done in a Zeiss Axio Observer 7 using bright

**Table 1** Compositions of studied materials (wt.%)

| Material | Cu | Li | Mg | Zr | Sc | Ag | Ti | V | Fe | Al | Others |
|---|---|---|---|---|---|---|---|---|---|---|---|
| TSc | 2.61 | 0.71 | 0.27 | 0.1 | 0.17 | 0.29 | 0.01 | 0.01 | 0.09 | 95.32 | Bal. |
| T | 2.52 | 0.72 | 0.27 | 0.12 | − | 0.33 | 0.02 | 0.02 | 0.09 | 95.99 | Bal. |

field (BF) imaging mode. Samples were polished with SiC papers and OPS colloidal silica suspension, then etched with a 0.5% HF solution in ethanol. Energy-dispersive X-ray spectroscopy (EDX) measurements, mapping, and back-scattered electron (BSE) and electron back-scattered diffraction (EBSD) imaging were done in the FEI Quanta scanning electron microscope (SEM). EBSD data were handled in the TSL OIM Analysis 8 software by EDAX. The software was used to create inverse pole figure (IPF) color-coded grain orientation maps. The software was also used to evaluate apparent grain diameters on particular cross-sections, assuming the equiaxed shape of grains. Samples for SEM measurement were mechanically polished with the OPS suspension and electrochemically etched with a 33% $HNO_3$ solution in methanol. Transmission electron microscopy and scanning transmission electron microscopy (TEM/STEM) observations were done in JEOL JEM 2000FX and JEOL JEM 2200 FS electron microscopes in bright field (BF) TEM and bright field and high-angle annular dark field (BF/HAADF) STEM modes. Samples for TEM/STEM were prepared in the form of 3 mm wide discs and electrolytically polished in a twin-jet TENUPOL V at −16 °C with a 33% $HNO_3$ solution in methanol. Statistical evaluation of TEM/STEM images was done in the ImageJ software. The microhardness of the material was measured with a QATM Qness Q10+ testing machine. Measurements were performed using the Vickers method with a load of 100 g and a load time of 10 s. Tensile tests were performed using an Instron 5882 testing machine at room temperature with a $10^{-3}$ $s^{-1}$ strain rate.

The as-cast materials were annealed in three steps at 300 °C for 30 min, 450 °C for 30 min, and 530 °C for 30 min, assuring the precipitation of fine dispersion of $Al_3Zr$ particles in the T alloy and $Al_3$(Sc,Zr) in the TSc alloy, and satisfactory homogeneous distribution of main strengthening elements (Cu, Li, Mg) in the matrix. The materials were then quenched into water at room temperature and artificially aged at 180 °C. This combined approach partially simulates the conventional T6 treatment of Al alloys. Microhardness was measured periodically during this aging process, and peak-aged conditions were established. Peak-aged samples annealed for 40 h taken along the rolling direction (RD), transversal direction (TD), and at 45° between them (45) were prepared for tensile testing. Three sets of samples for each material and direction were examined. One set of samples with the RD orientation was deformed in the as-cast state, and the other one was deformed immediately after solution treatment and quenching. Sample dimensions are given in Fig. 1.

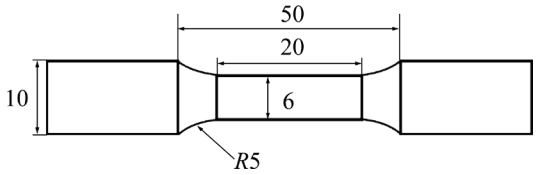


**Fig. 1** Schematic diagram of specimen for tensile tests (unit: mm)

## 3 Results

### 3.1 Microstructure of as-cast material

Particles formed during solidification are located along the boundaries of eutectic cells (Figs. 2(a, b)). These cells are smaller in the TSc material. The average dendrite spacing in this material is (12±1) μm as opposed to the dendrite

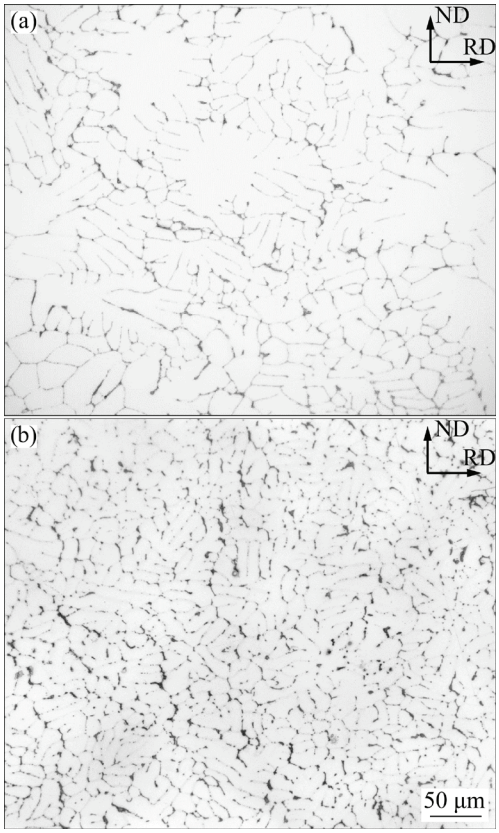


**Fig. 2** Microstructure of as-cast T (a) and TSc (b) materials in LOM images

spacing of (17±3) μm in T material. T material contains coarser grains with sizes ranging from 20 to 250 μm (Fig. 3(a)) and an average size of (90±55) μm. Smaller, more equiaxed grains are in the center, while larger elongated grains are located closer to the surface of the strip. Bimodal grain size and shape distributions are standard features of TRC materials [18]. The TSc material contains much finer grains, with EBSD-determined grain sizes ranging from 10 to 150 μm with an average size of (50±30) μm, with very fine grains in sections adjacent to the center (Fig. 3(b)). Graphs of apparent grain sizes in the studied cross-sections are shown in Fig. 3(c). Most TSc material grains have sizes below 50 μm, while the T material has a more even distribution of sizes up to 150 μm. A more detailed overview of the initial structure, including grain structures in different directions and heterogeneity of precipitation during TRC, can be found in Ref. [17]. Centerline segregation, a common type of macrosegregation, was also observed in the as-cast strips. However, in the case of actual industrial applications it could be reduced by further optimization of casting parameters.

Figure 4 shows the results of EDX mapping of the distribution of the main alloying elements. EDX cannot detect Li. Therefore, its distribution cannot be visualized by this method. However, Li-containing phases could be detected by diffraction methods [19]. Table 2 shows the results of EDX point analysis of selected particles from the BSE images in Fig. 4. The matrix always affects the results of point analysis of smaller particles. However, the majority of primary particles mainly contain Cu, Fe, and Mg and, in a limited manner, also Ag and Zr (and Sc in the case of the TSc material). The Fe-rich particles are most probably the $Al_7Cu_2Fe$ phase reported by CIESLAR et al [20]. BAJTOŠOVÁ et al [19] mention AlCu, $Al_2Cu$, $Al_2CuMg$, and $Al_2CuLi$ as the most frequent Fe-free boundary particles in both materials identified by diffraction methods. The Zr- and Sc-rich particles are most probably equilibrium trialuminides, which could generally not be dissolved during homogenization.

### 3.2 Structure of peak-aged materials

The homogenization/solution treatment of materials results in a substantial modification of the original dendritic structure and dissolution or transformation of most primary phase particles (Figs. 5(a, b)). There is no significant difference between the particle dispersion of T and TSc materials. The remaining particles have spherical or platelet-like morphologies typical for $Al_xFe(Cu)$ phases known from Al−Fe- and Al−Cu-based alloys containing Fe and Si as the minor admixtures [17,21,22]. Moreover, recent results by CIESLAR et al [20] received on the same alloy during in-situ TEM heating confirmed that Fe-rich $Al_7Cu_2Fe$ phases could not be fully dissolved even at 550 °C.

The T material is less resistant to the grain growth, and a distinct coarsening of grains could be observed after homogenization. The recrystallized grains have sizes ranging from 60 to 600 μm (Fig. 6(a)), and the average grain size is (330±160) μm. The TSc material only partially recrystallizing (Fig. 6(b)), contains numerous well-recovered subgrains, and its final grain size is

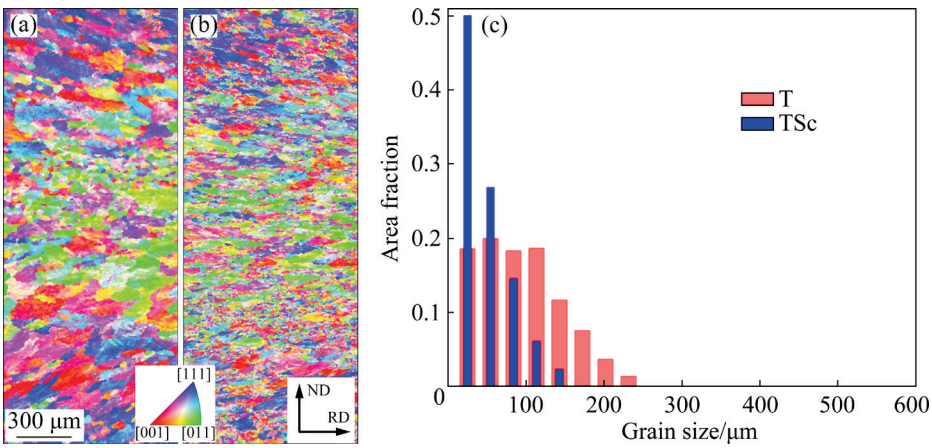


**Fig. 3** IPF grain shape and orientation maps of as-cast T (a) and TSc (b) materials, and histogram of apparent grain size in studied cross-section (c)

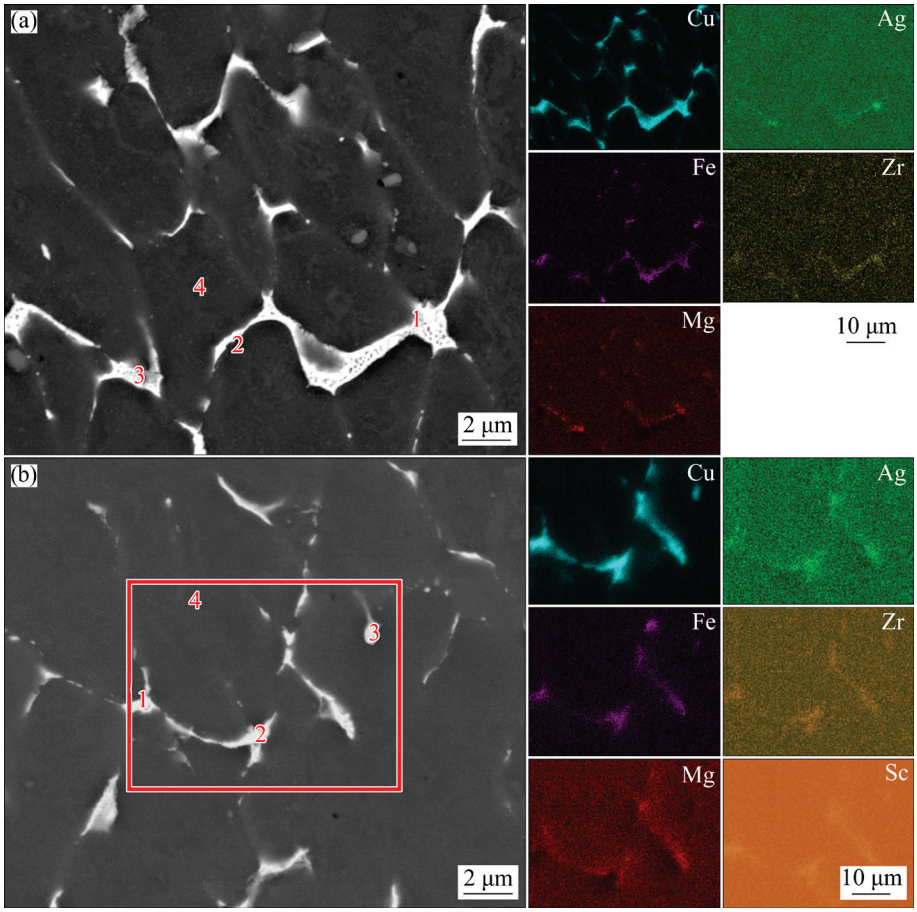


**Fig. 4** BSE images and EDX maps of area with higher amount of primary phase particles in as-cast T (a) and TSc (b) materials (The EDX area is highlighted for the TSc material)

**Table 2** Point EDX data of selected particles and particle-free matrix from Fig. 4 (at.%)

| Material | Location | Al | Cu | Fe | Mg | Ag | Zr | Sc |
|---|---|---|---|---|---|---|---|---|
| T | Particle 1 | 73.6 | 18.3 | 0.8 | 5.2 | 1.23 | 0.03 | 0 |
| | Particle 2 | 86.1 | 11.6 | 0.8 | 1.1 | 0.25 | 0.06 | 0 |
| | Particle 3 | 78.9 | 13.7 | 0.8 | 5.2 | 0.27 | 0.02 | 0 |
| | Matrix 4 | 98.3 | 0.4 | <0.1 | 0.9 | 0.25 | 0.04 | 0 |
| TSc | Particle 1 | 89.8 | 7.5 | 0.3 | 1.3 | 0.41 | 0.04 | 0.24 |
| | Particle 2 | 88.4 | 7.9 | 0.3 | 1.3 | 0.53 | 0.02 | 0.31 |
| | Particle 3 | 91.8 | 5.3 | 1.5 | 0.9 | 0.3 | 0.06 | 0.08 |
| | Matrix 4 | 98.1 | 0.4 | <0.1 | 1 | 0.22 | 0.05 | 0.09 |

substantially lower than that of the T material. Grain sizes are between 10 and 150 μm, which are the same as those of the as-cast material, but the distribution partially shifts towards larger grain sizes, and the average grain size is (65±40) μm (Fig. 6(c)).

The EDX analysis of processed specimens (Fig. 7 and Table 3) shows that persisting particles are almost entirely Al−Cu−Fe-based, most probably the $Al_7Cu_2Fe$ phase reported by CIESLAR et al [20] in the same alloy. Nevertheless, a limited number of Sc-containing (TSc material) particles and Al−Cu-based particles without Fe were also confirmed by EDX.

Nanoscale grain refining $Al_3Zr$ particles in the T material (Fig. 8(a)) and $Al_3(Sc,Zr)$ particles in the TSc (Fig. 8(b)) material precipitate during the heat treatment. BF STEM of the T material shows that

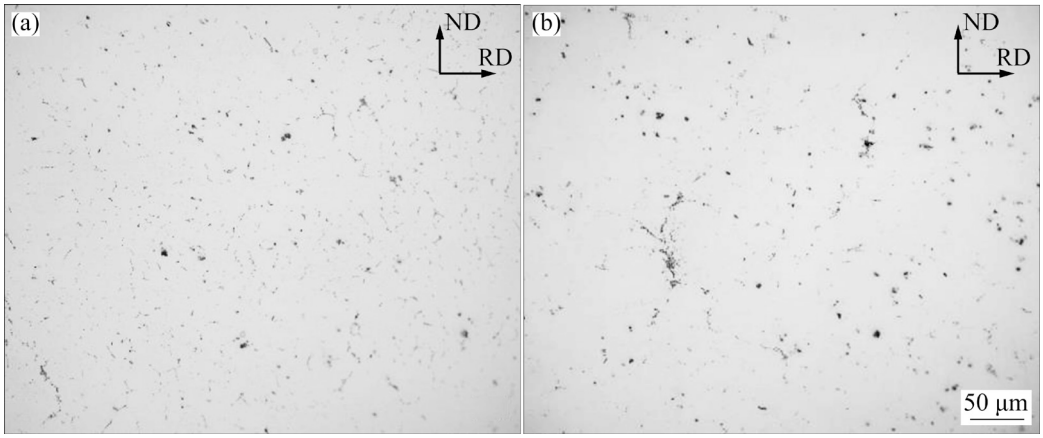


**Fig. 5** Undissolved particles in T (a) and TSc (b) materials after homogenization/solution treatment in LOM images

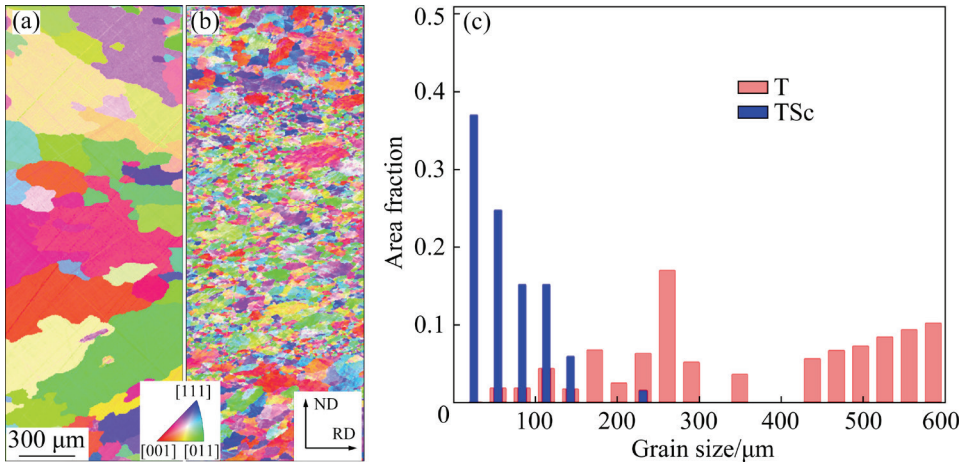


**Fig. 6** IPF grain shape and orientation maps of T (a) and TSc (b) materials after homogenization/solution treatment, and histogram of apparent cross-sectional grain size (c)

the $Al_3Zr$ particles are small, with a diameter of (2.4±0.7) nm. HAADF STEM of the TSc material shows the core−shell structure of the $Al_3(Sc,Zr)$ precipitates. $Al_3(Sc,Zr)$ particles are significantly coarser than the $Al_3Zr$ ones in the T material with a diameter of (9±1) nm. Strengthening $T_1(Al_2CuLi)$, $S'(Al_2CuMg)$, and $\theta'(Al_2Cu)$ precipitates appear after aging (Figs. 9(a−d)). $\theta'$ forms plates in $\{100\}_{Al}$ planes. $S'$ phase forms families of rods with their primary axis parallel to the $[100]_{Al}$ direction. However, our observations show that the $S'$ phase is a minor strengthening phase that precipitates with very low volume and number fractions. The $T_1$ phase precipitates as plates on $\{111\}_{Al}$ planes. These fixed orientation relations form additional reflections in diffractograms of the $[100]_{Al}$ and $[110]_{Al}$ zones. Schematic representations of these diffraction patterns are shown in Figs. 9(e, f) [3]. The SAED patterns in Figs. 9(a−d) confirm the presence of $T_1$ and $\theta'$ particles. $S'$ reflections are almost entirely suppressed due to a very low volume fraction of the $S'$ in the material.

### 3.3 Mechanical properties

The evolution of microhardness is very similar in both materials (Fig. 10). The first experimental points in Fig. 10(a) were measured immediately after homogenization/solution treatment and quenching. The initial microhardness after this treatment is around HV 80 without any increase within the experimental scatter during the first 1 h of aging. The first evident increase appears after 2 h of annealing at 180 °C. Maximum values were reached after 40 h of aging. Longer annealing time results in an overaging of the alloy and a slight decrease of microhardness in both alloys.

Figure 10(b) shows the engineering stress−strain ($\sigma$−$\varepsilon$) curves of both materials. Homogenized/solution-treated materials have superior formability, and their yield strengths are approximately 110 MPa.

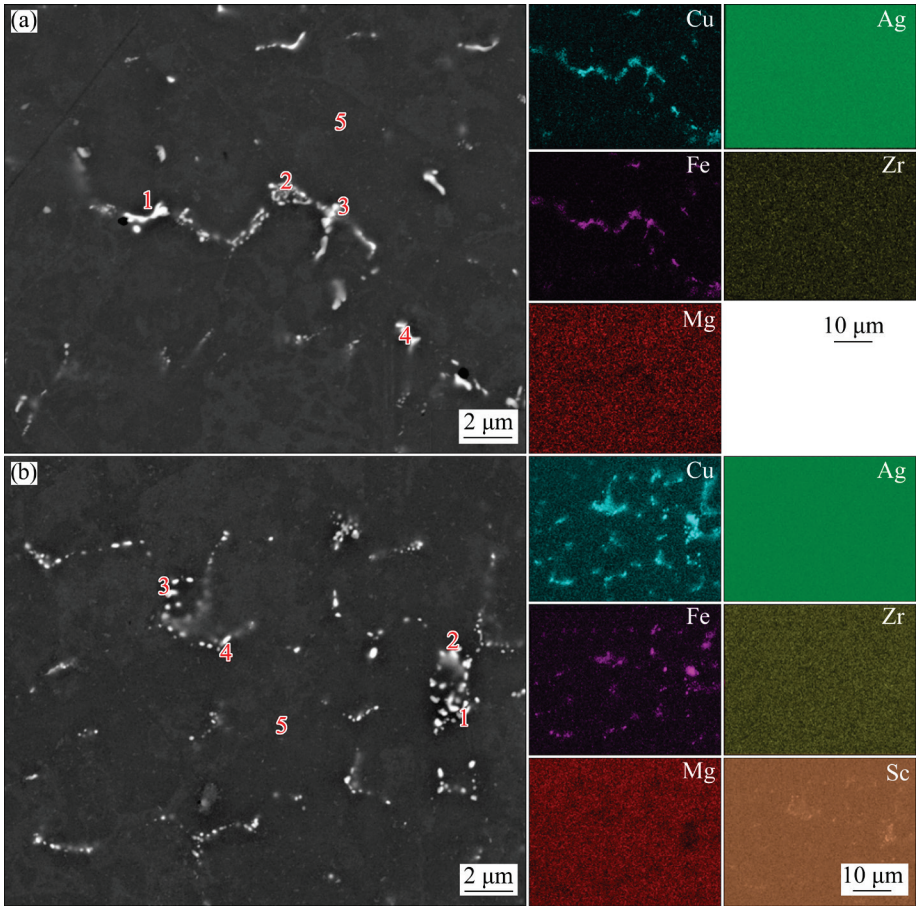


**Fig. 7** BSE image and EDX maps of major alloying elements in homogenized T (a) and TSc (b) materials in area with higher content of persisting particles

**Table 3** Point EDX data of selected particles and particle-free matrix from Fig. 7 (at.%)

| Material | Location | Al | Cu | Fe | Mg | Ag | Zr | Sc |
|---|---|---|---|---|---|---|---|---|
| T | Particle 1 | 88.9 | 7.5 | 2.3 | 0.8 | 0.22 | 0.03 | 0 |
| | Particle 2 | 91.7 | 5.2 | 1.7 | 0.8 | 0.26 | 0.03 | 0 |
| | Particle 3 | 89.9 | 6.7 | 2.1 | 0.8 | 0.21 | 0.04 | 0 |
| | Particle 4 | 89 | 7.2 | 2.3 | 0.9 | 0.27 | 0.03 | 0 |
| | Matrix 5 | 97.6 | 1.2 | <0.1 | 1 | 0.26 | 0.03 | 0 |
| TSc | Particle 1 | 94.1 | 2.1 | 0.2 | 0.7 | 0.36 | 0.04 | 0.24 |
| | Particle 2 | 90 | 4.7 | 1.5 | 0.8 | 0.25 | 0.03 | 0.11 |
| | Particle 3 | 91.4 | 6.2 | 0.1 | 0.8 | 0.25 | 0.03 | 0.66 |
| | Particle 4 | 93.9 | 3.8 | 0.3 | 0.9 | 0.27 | 0.02 | 0.31 |
| | Matrix 5 | 97.4 | 1.1 | <0.1 | 1.2 | 0.26 | 0.03 | 0.1 |

Moreover, both materials exhibit behavior associated with the Portevin-Le Chatelier effect above the yield point typical for this type of alloy after solution treatment [23]. The yield strength of homogenized/solution-treated materials is slightly higher than that of as-cast materials. The yield strength of peak-aged materials is between 290 and 325 MPa. However, their ductility is relatively low (less than 1%) and independent within the experimental error of the orientation on the specimen. The average values of the main mechanical properties are summarized in Table 4.

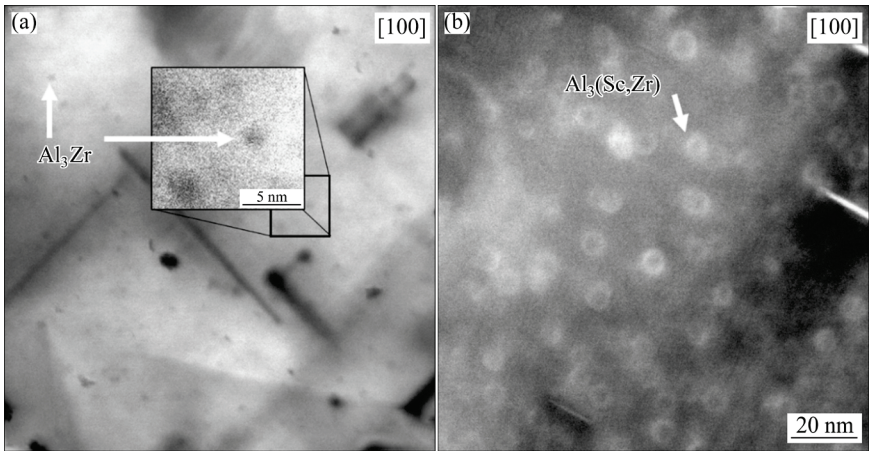


**Fig. 8** TEM images of peak-aged T (a) and TSc (b) materials: $Al_3Zr$ particles in BF STEM (a) and $Al_3(Sc,Zr)$ particles in HAADF STEM (b) close to $[100]_{Al}$

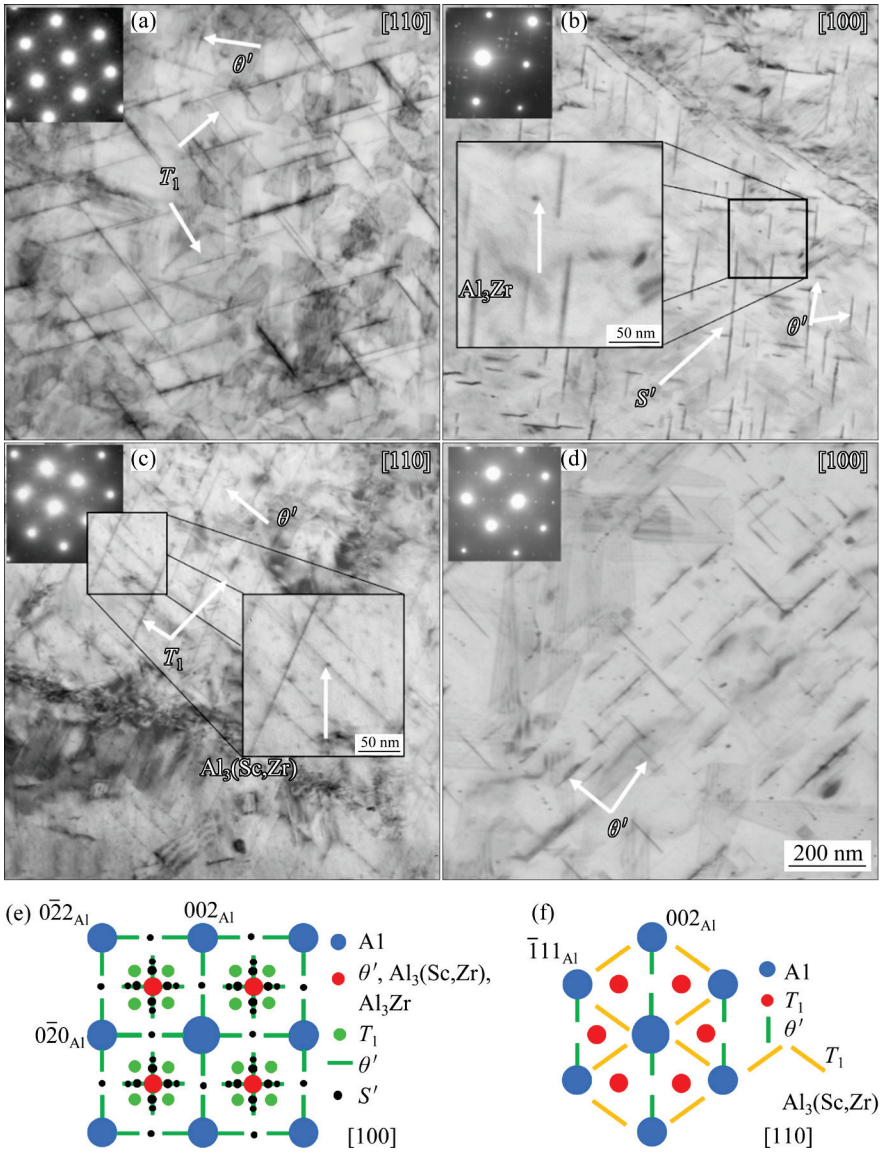


**Fig. 9** Strengthening particles of $T_1$ near $[110]_{Al}$, $\theta'$ and $S'$ close to $[100]_{Al}$ in BF TEM and corresponding SAED patterns (a–d), and schematic representations of $[100]_{Al}$ (e) and $[110]_{Al}$ (f) zone diffractograms containing main strengthening particles and dispersoids [3]

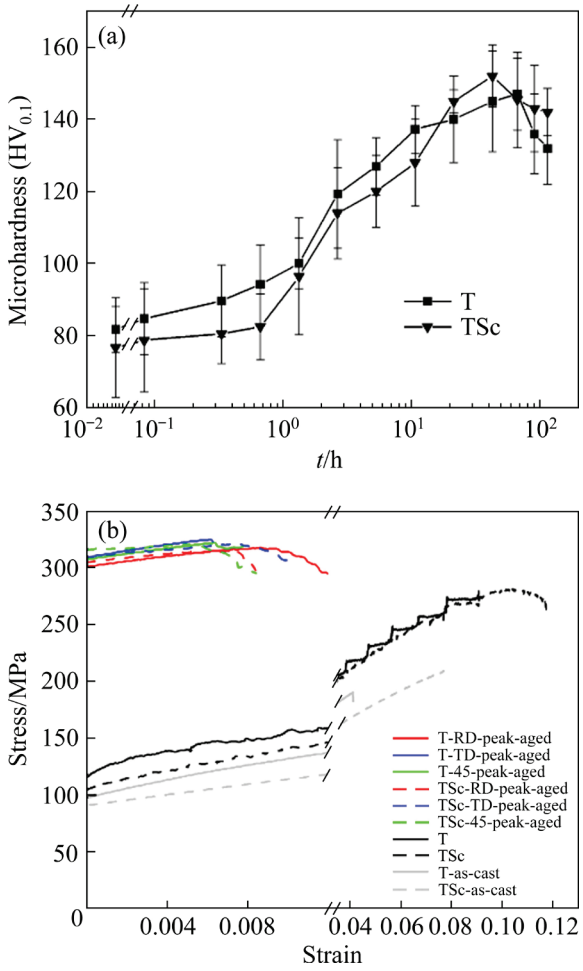


**Fig. 10** Microhardness evolution of T and TSC materials during aging at 180 °C (a), and engineering stress−strain curves of T and TSC materials in as-cast and homogenized/solution-treated states in rolling direction (RD) and peak-aged state after 40 h of artificial aging at 180 °C in rolling (RD), transversal (TD) directions and 45° (45) between RD and TD (b)

**Table 4** Average values of mechanical properties (T and TSc are in homogenized/solution-treated state)

| Sample | Yield strength/MPa | Ductility/% |
|---|---|---|
| T-RD-peak-aged | 294±7 | 0.9±0.3 |
| T-TD-peak-aged | 304±8 | 0.7±0.2 |
| T-45-peak-aged | 300±8 | 0.8±0.3 |
| T | 112±7 | 12±2 |
| T-as-cast | 97±6 | 4.1±1.2 |
| TSc-RD-peak-aged | 295±6 | 0.7±0.4 |
| TSc-TD-peak-aged | 297±9 | 1.0±0.4 |
| TSc-45-peak-aged | 303±17 | 0.6±0.2 |
| TSc | 106±6 | 9±2 |
| TSc-as-cast | 91±6 | 8±3 |

## 4 Discussion

A small addition of Sc in the TSc alloy shows only a limited impact on mechanical properties compared to the T material (Fig. 10 and Table 4). Although the influence of the Sc addition on the initial grain size, subsequent grain coarsening, and the size of trialuminides is significant, the strength and microhardness values in the homogenized/solution-treated and peak-aged states do not exhibit significant differences between both alloys.

The properties of homogenized/solution-treated materials are given mainly by the grain structure and the dispersion of trialuminides. The strength and microhardness of peak-aged alloys are given by a superposition of several main strengthening effects, including the already mentioned grain sizes and dispersion strengthening. Nevertheless, the role of strengthening $T_1$, $\theta'$, and $S'$ precipitates is dominant. However, the indirect impact of $Al_3Zr$ or $Al_3(Sc,Zr)$ dispersoids, grain boundaries, and the general substructure on the precipitation of other strengthening particles ($T_1$, $\theta'$ and $S'$ precipitates) should also be considered [24,25].

### 4.1 Effect of homogenization/solution treatment

There are two types of constituents in the twin-roll cast (TRC) materials. The first group contains Fe-rich primary or transformed coarse particles. They cannot fully dissolve in these materials, only transformed [20]. Of course, they can limit the ductility of the material. However, as they appear in the material due to Fe as a common impurity in Al alloys, their volume fraction could be decreased only by using higher purity input materials with a lower Fe content. Generally, their contribution to the final strengthening is relatively low (for example, ZHAO et al [26] estimated the value of dispersoid strengthening from these constituents around 5 MPa in an alloy with a 4% volume fraction of Fe-rich intermetallics), and they will not be considered in the following analysis.

The second group consists of Zr- and Sc-containing trialuminides. As reported by MARQUIS and SEIDMAN [27], binary $Al_3Sc$ particles precipitate usually below 350 °C. Annealing above 400 °C leads to a loss of coherency and coarsening above a diameter of 20 nm. Nevertheless, temperatures

above 400 °C are commonly applied to facilitating $Al_3Zr$ precipitation [8]. Therefore, according to ALGENDY et al [28], annealing at 300 °C and subsequently at 450 °C forms more stable core−shell ternary $Al_3(Sc,Zr)$ in the TSc material, preventing the coarsening of dispersoids even at 530 °C (Fig. 8). Thus, the ternary $Al_3(Sc,Zr)$ particles in the TSc alloy are still small, with a slightly larger diameter of (9±1) nm compared to the (2.4±0.7) nm diameter of $Al_3Zr$ particles in the T alloy (Figs. 8(a, b)). Dispersoid size was determined based on two STEM micrographs. The total amounts of Zr and Zr + Sc are 0.12 wt.% and 0.27 wt.% in the T and TSc materials, respectively. The maximum volume fractions of Sc and Zr-containing particles, assuming that all Sc and Zr atoms could precipitate in the form of their respective trialuminides, are 0.12% in the T material and 0.52% in the TSc material (LI et al [29] estimated the volume fraction of $Al_3Zr$ to be 0.06%−0.70% in the material containing 0.12 wt.% Zr depending on homogenization conditions, BELOV et al [30] reported a 0.5% volume fraction of $Al_3(Sc,Zr)$ in an alloy with 0.1 wt.% Sc and 0.2 wt.% Zr). Based on the equation reported by LIU et al [31], their contribution can be estimated as follows:

$$\sigma_{OR}=0.4MGb\ln\left(\frac{d}{b}\right)\cdot\frac{1}{0.5d\pi\sqrt{1-\upsilon}\left(\sqrt{\left(\frac{3\pi}{4f}\right)}-1.64\right)} \quad (1)$$

where $d$ and $f$ are particle diameter and volume fraction, respectively, $G$ is shear modulus (25.4 GPa for Al), $b$ is the amplitude of Burgers vector (0.286 nm), $\upsilon$ is the Poisson ratio (0.33), $M$ is the Taylor factor (≈3.06 for FCC materials). Calculation of the strengthening effect of trialuminides based on experimentally measured diameters of (2.4±0.7) nm and (9±1) nm, and estimated volume fractions of 0.12% and 0.52% for the $Al_3Zr$ and $Al_3(Sc,Zr)$ particles, respectively, yields (58±16) MPa for $Al_3Zr$ and (72±8) MPa for $Al_3(Sc,Zr)$. The values are the same within the experimental error because the larger $Al_3(Sc,Zr)$ particles in the TSc alloy with a substantially higher volume fraction have their contribution to Orowan strengthening per particle lower than the one calculated for $Al_3Zr$ particles.

The ternary trialuminide also provides a more substantial anti-recrystallization effect than the binary $Al_3Zr$ due to the more favorable interaction energy of the precipitate/matrix interface. LIU et al [32] concluded that the interface energy of the $\alpha$(Al)(111)/$Al_3(Sc,Zr)$(111) interface is lower than that of the $\alpha$(Al)(111)/$Al_3Zr$(111) interface, which further promotes grain refinement. This results in higher recrystallization and grain growth resistance observed in the TSc material (Compare with Figs. 6(a, b)).

The grain refinement could lead to an increase in strength following the Hall−Petch relationship:

$$\sigma_{HP}=kd_g^{-1/2} \quad (2)$$

where $\sigma_{HP}$ is the Hall−Petch contribution to strength, $k$ is a coefficient equal to 0.04 MPa·m$^{1/2}$ for Al, and $d_g$ is the grain diameter [33]. The estimated values of the Hall−Petch strengthening of the T and TSc materials are (2.5±0.7) and (6.2±0.7) MPa, respectively. The calculations are based on average grain sizes determined by the linear line average intercept method from EBSD images with high-angle grain boundaries (misorientation angle >15°) of homogenized/solution-treated materials. Intercepting line length divided by the number of intercepted grains is multiplied by a factor (1.56 for polyhedral grains [34]) accounting for the difference between true grain diameter and the diameter of a random grain section in the observation plane. The final values used in Eq. (2) are (255±75) and (38±4) μm for the T and TSc materials, respectively (Fig. 6(c)). Grain size values were reevaluated using the circular intercept method for the purposes of the calculation. There is a relatively low difference in the Hall−Petch contribution to strength of both alloys in the homogenized/solution-treated state due to relatively high grain sizes of both alloys. The calculated gap (17±4) MPa thus validates the low impact of the Sc addition observed in this state.

### 4.2 Effect of artificial aging

The essential consequence of the new annealing scheme is the almost complete dissolution of Fe-free primary particles containing main age-hardening constituents (Cu, Mg, Li), limitation of Li evaporation (FOX et al [35] studied an alloy with

2.6 wt.% Li and observed 20 wt.% of the Li content at 50 μm below the surface and half the Li content at 100 μm below the surface after 4 h annealing at 530 °C), and a maximal super-saturation of the matrix before the artificial aging step. For example, the content of Cu in the solution-treated matrix measured by EDS is around 2.6 wt.% (see Table 1), which is almost the same as the total content of Cu in the material.

The following paragraph estimates the contribution of $T_1$ and $\theta'$ particles to the total strength of both materials in peak-aged conditions. The influence of the $S'$-phase is not considered due to a very low fraction of this phase observed by electron microscopy. Strengthening by the $T_1$ phase ($\sigma_{OR}$) can be calculated from the model of DORIN et al [36], assuming a square root relation of $T_1$ strengthening on the volume fraction:

$$\sigma_{OR}=\frac{1.211d\gamma^{3/2}}{t^2}\sqrt{\frac{bf}{\Gamma}} \tag{3}$$

where $t$ is precipitate thickness, $\gamma$ is the interfacial energy, and $\Gamma$ is dislocation line tension, approximated as $1/2Gb^2$. A modification of Eq. (4) by BAHL et al [37] enables to calculate the strengthening contribution of $\theta'$:

$$\sigma_{OR}=\frac{MGb}{2\pi\sqrt{1-\upsilon}}\left(\frac{1}{\lambda}\right)\ln\left(\frac{0.981\sqrt{dt}}{b}\right) \tag{4}$$

where $\lambda$ is interparticle spacing which can be calculated as

$$\lambda=\frac{1.267}{\sqrt{N_f d}}-\frac{\pi d}{8}-1.061t \tag{5}$$

where $N_f$ is the particle number fraction defined as the number of $\theta'$ particles per unit sample volume. Particle number and volume fractions in the studied materials can be determined from TEM images (Fig. 9) after establishing the thickness of the TEM sample. The thickness of the foil was determined through convergent beam electron diffraction (CBED), as described by KELLY et al [38]. The volume fraction of a specific type of particle can, in principle, be calculated as

$$f=\frac{N_p V_p}{V_s} \tag{6}$$

where $N_p$ is the number of particles in an observed area, $V_p$ is the average volume of a single particle, and $V_s$ is the volume of the observed zone.

Both $T_1$ and $\theta'$ particles are supposed to have a disc shape. $T_1$ particles have larger diameters than the thickness of the observed area (≈100 nm). Therefore, the measured length of these particles is, in the first approximation, assumed to be equal to their actual diameter. In the case of $\theta'$ particles, their diameter is calculated as

$$d=d_m\frac{(d_m+t_s)}{(\frac{\pi}{4}d_m+t_s)} \tag{7}$$

where $d_m$ is the measured particle length, and $t_s$ is the sample thickness obtained by CBED. The total volume fraction of all $T_1$ particles ($f_{VT}$) is calculated as

$$f_{VT}=2\frac{t_s dtN_p}{V_s} \tag{8}$$

The factor of 2 is added to include the remaining two independent families of $T_1$ precipitates. The volume fraction of all $\theta'$ particles ($f_{V\theta'}$) is calculated as

$$f_{V\theta'}=1.5\frac{t_s d^2 tN_p}{4V_s}k \tag{9}$$

We estimate that the entire disc of the precipitate contributes to the volume fraction in the observed part of the specimen. The factor of 1.5 is added to include the remaining third family of $\theta'$, which is not observed edge-on in the specific [100] orientation. All possible planes of habitat are assumed to be equally populated for both types of particles. $k$ is added as a coefficient of the contribution of individual $\theta'$ discs to the total volume. The value of this coefficient could be estimated as

$$k=\frac{t_s}{t_s+d} \tag{10}$$

In the case of $T_1$ particles, this estimated volume fraction is the upper possible limit. The values estimated from the TEM and STEM observations are summarized in Table 5.

However, electron microscopy is generally an extremely local method and might not provide sufficiently relevant statistics. Considering all these factors, the calculated volume fraction could be higher than the real one. For example, values shown in Table 5 correspond to a total Cu content close to 4.3 wt.% (the real one is ~2.7 wt.%). An estimation

of the highest possible volume fractions of particles was made to fix this discrepancy. We assume that all the remaining Cu and Li atoms in the matrix could precipitate as strengthening particles considering the solubility limits of ~0.25 wt.% for Cu and ~0.35 wt.% for Li [39,40] at the aging temperature (180 °C). Keeping the volume fraction ratio of $T_1$ and $\theta'$ the same as in the previous calculations, the final results could be modified into a form summarized in Table 6.

**Table 5** Parameters of strengthening particles and their contributions to strength ($\sigma$ is their strengthening contribution)

| Material | Particle | $N_p$ | $d$/nm | $t$/nm | $f$/% | $\sigma$/MPa |
|---|---|---|---|---|---|---|
| T | $T_1$ | 66 | 274±60 | 3.2±0.7 | 3.9±1.2 | 129±48 |
| | $\theta'$ | 117 | 76±13 | 5.8±1.1 | 0.8±0.2 | 47±14 |
| TSc | $T_1$ | 85 | 228±61 | 2.7±0.5 | 4.0±1.3 | 137±52 |
| | $\theta'$ | 80 | 138±29 | 6±1.0 | 0.7±0.2 | 49±16 |

**Table 6** Parameters of strengthening particles and their contributions to final strength ($f_c$ and $\sigma_c$ are volume fractions and strengthening contributions after correction, respectively)

| Material | Particle | $d$/nm | $t$/nm | $f_c$/% | $\sigma_c$/MPa |
|---|---|---|---|---|---|
| T | $T_1$ | 274±60 | 3.2±0.7 | 3.9±1.2 | 129±48 |
| | $\theta'$ | 76±13 | 5.8±1.1 | 0.8±0.2 | 47±14 |
| TSc | $T_1$ | 228±61 | 2.7±0.5 | 4.0±1.3 | 137±52 |
| | $\theta'$ | 138±29 | 6±1.0 | 0.7±0.2 | 49±16 |

The total strength increase during aging estimated in our calculations is slightly lower than that shown in Fig. 10 (around 200 MPa). However, considering the scatter due to all the estimations made in our calculations, these results confirm a good agreement between observed microstructures and the measured increase of strength imposed by aging.

Industrial DC-cast AA2195 and other Al−Cu−Li-based alloys with similar Cu and Li contents generally exhibit higher yield and tensile strengths (yield strength of 560 MPa and tensile strength over 600 MPa), higher microhardness increase during artificial aging (HV 190) and also better ductility (~8%) [29,41−47]. However, these alloys typically contain significantly higher content of alloying elements (standard AA2195 alloys contain ~4 wt.% Cu, ~1 wt.% Li, and ~0.6 wt.%Mg) and finer microstructure (substructure) due to necessary rolling steps. Generally, the peak mechanical properties are reported in the T8 temper rather than in the T6 one. Values of the yield strength reported for the T6 temper [42−45] are always lower, and despite a higher content of alloying elements, they are comparable to the ones measured in our experiments. Also, several attempts to add Sc were accomplished in ingot-cast Al−Cu−Li-based materials [4,47,48]. However, the positive role of this addition was questionable. Usually, the unavoidable homogenization treatment, which should be performed at high temperatures and long soaking time, results in a significant coarsening of $Al_3$(Sc,Zr) particles above the coherency limit (20 nm) [30]. Consequently, their ability to inhibit grain growth during additional thermomechanical treatment is lost. These long homogenization soaking time is not required for the continuously cast near-net-shaped strip. Possible macro-segregation occurs on the order of magnitude lower scales due to faster solidification of the cast strip. The same applies to microsegregation due to the different sizes of solidified eutectic cells. To illustrate this, a LOM micrograph comparison of the TRC material and an experimentally mold-cast ingot of the same alloy in the as-cast state is shown in Fig. 11. While particle spacing in the mold-cast material is around 150 μm, the secondary dendrite arm spacing in the TRC material is around 15 μm. Particles in the TRC material are also considerably finer and therefore dissolve faster during high temperature heat treatment.

The processing route proposed in the current study consisting of a near-net shape manufacturing of thin strips and a three-step procedure combining homogenization and solution treatment into one short step limits the unfavorable influence of this high-temperature exposure. Limited Li evaporation and dispersion of relatively small $Al_3$(Sc,Zr) particles enable the exploitation of the potential of Sc addition in Al−Li−Cu−Mg−Zr-based alloys. Thus, the proposed route could be further modified (pre-stretching prior to artificial aging, severe plastic deformation during the formation of trialuminides for grain refinement, etc.), further improving the strength and ductility of the strip.

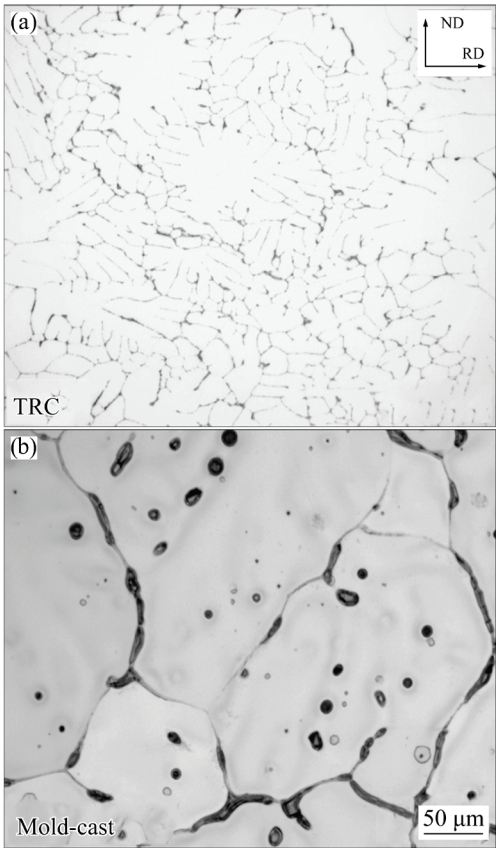


**Fig. 11** LOM micrographs of TRC material (a) and experimental mold-cast ingot (b) of same T alloy in as-cast state

## 5 Conclusions

(1) Sc provides a strong grain refining effect already in the as-cast state. Grains in the Sc-free alloy prepared by the same route have almost twice as large diameters.

(2) Particles of the $Al_3(Sc,Zr)$ phase form a fine dispersion during combined annealing at 300 and 450 °C. Their significant coarsening does not occur at higher temperatures, and they efficiently inhibit recrystallization and grain growth during annealing at 530 °C. Particles of the $Al_3Zr$ phase precipitating in the Sc-free alloy could not sufficiently hinder the grain boundary motion at high temperatures, and substantial grain growth occurs in this alloy at 530 °C.

(3) The impact of the Sc addition on the yield strength of the homogenized and peak-aged material is minimal. Calculated contributions of $Al_3(Sc,Zr)$ particles to the strength through Orowan strengthening or indirectly through the Hall−Petch strengthening are relatively low. Nevertheless, their potential to hinder grain growth and preserve fine-grained structure makes them excellent candidates for further refining TRC Al−Cu−Li−Mg−Zr alloys.

### CRediT authorship contribution statement

**Rostislav KRÁLÍK:** Writing – Original draft preparation, Investigation, Validation; **Barbora KŘIVSKÁ:** Investigation, Writing – Review and editing; **Lucia BAJTOŠOVÁ:** Investigation, Visualization, Validation; **Mykhailo STOLBCHENKO:** Resources; **Mirko SCHAPER:** Supervision; **Olexandr GRYDIN:** Supervision, Resources, Conceptualization; **Miroslav CIESLAR:** Supervision, Writing − Review and editing, Conceptualization.

### Declaration of competing interest

The authors declare that they have no known competing financial interests or personal relationships that could have appeared to influence the work reported in this paper.

### Acknowledgments

The authors would like to thank the project of the Czech Science Foundation (No. 20-19170S) and the German Research Foundation (Deutsche Forschungsgemeinschaft (DFG)) for financial support within the scope of project (No. SCHA 1484/46-1).

### References

[1] LAVERNIA E J, GRANT N J. Aluminium−lithium alloys [J]. Journal of Materials Science, 1987, 22: 1521−1529.

[2] WANG S C, STARINK M J. Precipitates and intermetallic phases in precipitation hardening Al–Cu–Mg–(Li) based alloys [J]. International Materials Reviews, 2005, 50: 193−215.

[3] HAUSLER I, SCHWARZE C H, BILAL M U, RAMIREZ D V, HETABA W, KAMACHALI R D, SKROTZKI B. Precipitation of $T_1$ and $\theta'$ phase in Al−4Cu−1Li−0.25Mn during age hardening: Microstructural investigation and phase-field simulation [J]. Materials, 2017, 10: 112.

[4] SURESH M, SHARMA A, MORE A M, NAYAN N, SUWAS S. Effect of scandium addition on evolution of microstructure, texture and mechanical properties of thermo-mechanically processed Al−Li alloy AA2195 [J]. Journal of Alloys and Compounds, 2018, 740: 364−374.

[5] FINK D, HNATOWICZ D, KVITEK J, HAVRANEK V, ZHOU J T. External oxidation of aluminium−lithium alloys [J]. Surface and Coatings Technology, 1992, 51: 57−64.

[6] KIM J H, JEUN J H, CHUN H J, LEE R J, YOO J T, YOON J H, LEE H S. Effect of precipitates on mechanical properties of AA2195 [J]. Journal of Alloys and Compounds, 2016, 669: 187−198.

[7] JIN Y Y, YU H P. Enhanced formability and hardness of AA2195-T6 during electromagnetic forming [J]. Journal of Alloys and Compounds, 2022, 890: 161891.
[8] KNIPLING K E, DUNAND D C, SEIDMAN D N. Precipitation evolution in Al–Zr and Al–Zr–Ti alloys during aging at 450−600 °C [J]. Acta Materialia, 2008, 56: 1182−1195.
[9] TIAN S K, LI J Y, ZHANG J L, WULABIEKE Z, LV D. Effect of Zr and Sc on microstructure and properties of 7136 aluminum alloy [J]. Journal of Materials Research and Technology, 2019, 8: 4130−4140.
[10] MURRAY J L. The Al−Sc (aluminum−scandium) system [J]. Journal of Phase Equilibria, 1998, 19: 380−384.
[11] XU P, JIANG F, TANG Z Q, YAN N, JIANG J Y, XU X, PENG Y. Coarsening of $Al_3Sc$ precipitates in Al−Mg−Sc alloys [J]. Journal of Alloys and Compounds, 2019, 781: 209−215.
[12] LI S, JIANG T, WANG J Y, CHEN L Z, WEI B W, LI Y, XU G M, WANG Z D. Effects of different external fields on the microstructure and mechanical properties of novel Al−Cu−Li alloy during twin-roll casting [J]. Materials Science and Engineering A, 2019, 757: 14−22.
[13] LI S J, HE C, FU J Y, XU J J, XU G M, WANG Z D. Evolution of microstructure and properties of novel aluminum−lithium alloy with different roll casting process parameters during twin-roll casting [J]. Materials Characterization, 2020, 161: 110145.
[14] LI Y, LI S J, WEI B W, XU J J, LIAN J H, XU G M, WANG Z D. Microstructural evolution and properties of electromagnetic cast-rolled novel Al−Li alloy under different heat treatment procedures [J]. Journal of Materials Research and Technology, 2022, 16: 864−878.
[15] BAREKAR N S, DHINDAW B K. Twin-roll casting of aluminum alloys — An overview [J]. Materials and Manufacturing Processes, 2014, 29: 651−661.
[16] FORBORD B, LEFEBVRE W, DANOIX F, HALLEM H, MARTHINSEN K. Three dimensional atom probe investigation on the formation of $Al_3$(Sc,Zr)-dispersoids in aluminium alloys [J]. Scripta Materialia, 2004, 51: 333−337.
[17] GRYDIN O, STOLBCHENKO M, SCHAPER M, BELEJOVÁ S, KRÁLÍK R, BAJTOŠOVÁ L, KŘIVSKÁ B, HÁJEK M, CIESLAR M. New twin-roll cast Al−Li based alloys for high-strength applications [J]. Metals, 2020, 10: 987.
[18] KRÁLÍK R, KŘIVSKÁ B, BAJTOŠOVÁ L, ŠLAPÁKOVÁ M, CIESLAR M. Homogenization of twin-roll cast AA8079 aluminum alloy studied by in-situ TEM [J]. Transactions of Nonferrous Metals Society of China, 2022, 32: 2138−2149.
[19] BAJTOŠOVÁ L, GRYDIN O, STOLBCHENKO M, SCHAPER M, KŘIVSKÁ B, KRÁLÍK R, ŠLAPÁKOVÁ M, CIESLAR M. Phase identification in twin-roll cast Al−Li alloys [C]//Proceedings of the 31st International Conference on Metallurgy and Materials. Ostrava, CZE: Tanger Ltd., 2022: 587−592.
[20] CIESLAR M, KŘIVSKÁ B, KRÁLÍK R, BAJTOŠOVÁ L, GRYDIN O, STOLBCHENKO M, SCHAPER M. Homogenization of twin-roll cast Al−Li-based alloy studied by in-situ electron microscopy [C]//Proceedings of the 31st International Conference on Metallurgy and Materials. Ostrava, CZE: Tanger Ltd., 2022: 593−598.
[21] ZHANG L F, GAO J W, DAMOAH L N W, ROBERTSON D G. Removal of iron from aluminum: A review [J]. Mineral Processing and Extractive Metallurgy Review, 2012, 33: 99−157.
[22] GAO Y H, KUANG J, LIU G, SUN J. Effect of minor Sc and Fe co-addition on the microstructure and mechanical properties of Al−Cu alloys during homogenization treatment [J]. Materials Science and Engineering A, 2019, 746: 11−26.
[23] HU Z H, QI Y, NIE X J, ZHANG H, ZHU H H. The Portevin-Le Chatelier (PLC) effect in an Al−Cu aluminum alloy fabricated by selective laser melting [J]. Materials Characterization, 2021, 178: 111198.
[24] JIANG B, WANG H S, YI D Q, TIAN Y, SHEN F H, WANG B, LIU H Q, HU Z. Effect of Ag addition on the age hardening and precipitation behavior in an Al−Cu−Li−Mg−Zn−Mn−Zr alloy [J]. Materials Characterization, 2020, 162: 110184.
[25] DORIN T, RAMAJAYAM M, VAHID A, LANGAN T. Fundamentals of aluminum metallurgy: Aluminum−scandium alloys [M]. Amsterdam: Elsevier Ltd., 2018: 439−494.
[26] ZHAO Y L, ZHANG W W, YANG C, ZHANG D T, WANG Z. Effect of Si on Fe-rich intermetallic formation and mechanical properties of heat-treated Al–Cu–Mn–Fe alloys [J]. Journal of Materials Research, 2018, 33: 898−911.
[27] MARQUIS E A, SEIDMAN D N. Nanoscale structural evolution of $Al_3Sc$ precipitates in Al(Sc) alloys [J]. Acta Materialia, 2001, 49: 1909−1919.
[28] ALGENDY A Y, LIU K, ROMETSCH P, PARSON N, CHEN X G. Evolution of discontinuous/continuous $Al_3$(Sc,Zr) precipitation in Al−Mg−Mn 5083 alloy during thermomechanical process and its impact on tensile properties [J]. Materials Characterization, 2022, 192: 112241.
[29] LI Y, LU B, YU W, FU J Y, XU G M, WANG Z D. Two-stage homogenization of Al−Zn−Mg−Cu−Zr alloy processed by twin-roll casting to improve L12 $Al_3Zr$ precipitation, recrystallization resistance, and performance [J]. Journal of Alloys and Compounds, 2021, 882: 160789.
[30] BELOV N A, ALABIN A N, ESKIN D G, ISTOMIN-KASTROVSKII V V. Optimization of hardening of Al–Zr–Sc cast alloys [J]. Journal of Materials Science, 2006, 41: 5890−5899.
[31] LIU Q B, FAN G L, TAN Z Q, LI Z Q, ZHANG D, WANG J, ZHANG H. Precipitation of $Al_3Zr$ by two-step homogenization and its effect on the recrystallization and mechanical property in 2195 Al–Cu–Li alloys [J]. Materials Science and Engineering A, 2021, 821: 141637.
[32] LIU Y, ZHANG C C, ZHANG X Y, HUANG Y C. Understanding grain refinement of Sc addition in a Zr containing Al−Zn−Mg−Cu aluminum alloy from experiments and first-principles [J]. Intermetallics, 2020, 123: 106823.
[33] XUE S C, LI Q, FAN Z, WANG H, ZHANG Y F, DING J, WANG H Y, ZHANG X H. Strengthening mechanisms and deformability of nanotwinned AlMg alloys [J]. Journal of Materials Research, 2018, 33: 3739−3749.
[34] MENDELSON M I. Average grain size in polycrystalline

ceramics [J]. Journal of the American Ceramic Society, 1969, 52: 443−446.
[35] FOX S, FLOWER H M, MCDARMAID D S. Oxidation induced solute depletion in Al−Cu−Mg−Li alloys [J]. Scripta Metallurgica, 1986, 20: 71−74.
[36] DORIN T, DESCHAMPS A, de GEUSER F, SIGLI C. Quantification and modelling of the microstructure/strength relationship by tailoring the morphological parameters of the $T_1$ phase in an Al–Cu–Li alloy [J]. Acta Materialia, 2014, 75: 134−146.
[37] BAHL S, XIONG L H, ALLARD L F, MICHI R A, POPLAWSKY J D, CHUANG A C, SINGH D, WATKINS T R, SHIN D, HAYNES J D, SHYAM A. Aging behavior and strengthening mechanisms of coarsening resistant metastable $\theta'$ precipitates in an Al–Cu alloy [J]. Materials & Design, 2021, 198: 109378.
[38] KELLY P M, JOSTSONS A, BLAKE R G, NAPIER J G. The determination of foil thickness by scanning transmission electron microscopy [J]. Physica Status Solidi, 1975, 31: 771−780.
[39] STEFANESCU D M, RUXANDA R. Alloy phase diagrams [M]. Ohio: ASM International, 1992.
[40] AUGUSTYN-PIENIAZEK J, ADRIAN H, RZADKOSZ S, CHOROSZYNSKI M. Structure and mechanical properties of Al−Li alloys as cast [J]. Archives of Foundry Engineering, 2013, 13: 5−10.
[41] RODGERS B I, PRANGNELL P B. Quantification of the influence of increased pre-stretching on microstructure−strength relationships in the Al–Cu–Li alloy AA2195 [J]. Acta Materialia, 2016, 108: 55−67.
[42] LIN Y, LU C G, WEI C Y, ZHENG Z Q. Effect of aging treatment on microstructures, tensile properties and intergranular corrosion behavior of Al–Cu–Li alloy [J]. Materials Characterization, 2018, 141: 163−168.
[43] GABLE B M, ZHU A W, CSONTOS A A, STARKE E A. The role of plastic deformation on the competitive microstructural evolution and mechanical properties of a novel Al–Li–Cu–X alloy [J]. Journal of Light Metals, 2001, 1: 1−14.
[44] CASSADA W A, SHIFLET G J, STARKE E A. The effect of plastic deformation on $Al_2CuLi$($T_1$) precipitation [J]. Metallurgical Transactions A, 1991, 22: 299−306.
[45] DUAN S W, GUO F Q, ZHANG Y A, CHONG K, LEE S, MATSUDA K, ZOU Y. Effects of texture and precipitates characteristics on anisotropic hardness evolution during artificial aging for an Al–Cu–Li alloy [J]. Materials & Design, 2021, 212: 110216.
[46] MA P P, ZHAN L H, LIU C H, WANG Q, LI H, LIU D B, HU Z. Pre-strain-dependent natural ageing and its effect on subsequent artificial ageing of an Al−Cu−Li alloy [J]. Journal of Alloys and Compounds, 2019, 790: 8−19.
[47] ZHANG J S, WU G H, ZHANG L, ZHANG X L, SHI C C, TONG X. Addressing the strength-ductility trade-off in a cast Al−Li−Cu alloy—Synergistic effect of Sc-alloying and optimized artificial ageing scheme [J]. Journal of Materials Science & Technology, 2022, 96: 367−382.
[48] JIANG B, YI D Q, YI X Q, ZHENG F, WANG H S, WANG B, LIU H Q, HU Z. Effect of trace amounts of added Sc on microstructure and mechanical properties of 2055 aluminum alloy [J]. Materials Characterization, 2018, 141: 248−259.

# Sc 元素添加对双辊铸轧 Al−Cu−Li−Mg−Zr 基合金热处理的影响

Rostislav KRÁLÍK[1], Barbora KŘIVSKÁ[1], Lucia BAJTOŠOVÁ[1],
Mykhailo STOLBCHENKO[2], Mirko SCHAPER[2], Olexandr GRYDIN[2], Miroslav CIESLAR[1]

1. Department of Physics of Materials, Faculty of Mathematics and Physics,
Charles University, Ke Karlovu 5, 12116, Prague, Czech Republic;
2. Department of Materials Science, Faculty of Mechanical Engineering,
University of Paderborn, Warburger Straße 100, 33098, Paderborn, Germany

**摘　要**：提出制备含 Sc 的 Al−Cu−Li−Mg−Zr 基合金带材的工艺方案。即先采用双辊铸轧技术制备近净形状的 3 mm 厚带材，再对其进行均匀化/固溶处理。研究两种 Al−Cu−Li−Mg−Zr 基双辊铸轧合金，其中一种添加质量分数为 0.17%的 Sc，另一种未添加 Sc。两种合金均先在 300 ℃下退火 30 min，然后在 450 ℃下退火 30 min 以及 530 ℃下退火 30 min，随后进行室温水淬。前两段退火后组织中生成了细小、弥散的 $Al_3Zr$/$Al_3$(Sc,Zr) 颗粒。最后的退火步骤起到了均匀化/固溶处理的作用。双辊铸轧材料的细小晶粒结构使含有主要合金元素的原始颗粒在较短的退火时间内溶解。缩短保温时间可以限制表面层中 Li 的耗尽和 $Al_3Zr$/$Al_3$(Sc,Zr)弥散相的明显粗化。铸态含 Sc 材料已经具有明显细小的晶粒结构，而经均匀化/固溶处理后生成的 $Al_3$(Sc,Zr)弥散相抑制了晶粒在高温下发生粗化。在后续 180 ℃下时效处理后，形成了 $\theta'$($Al_2Cu$)、$T_1$($Al_2CuLi$)和 $S'$($Al_2CuMg$) 强化相。在峰值时效状态下，屈服强度提高了 200 MPa，这一数值与类似直接冷却铸造材料的相当，从而证实了所提方案的合理性。

**关键词**：显微组织；力学性能；Al−Cu−Li 基合金；Sc 合金化；双辊铸轧

**(Edited by Wei-ping CHEN)**